35th AIAA Fluid Dynamics Conference and Exhibit
6 - 9 June 2005, Toronto, Ontario Canada

AIAA 2005-5143

Design of a Wave-Rotor Transition Duct

John W. Slater*
NASA Glenn Research Center at Lewis Field, Brook Park, Ohio, 44135

and

Gerard E. Welch†
U.S. Army Research Laboratory, Vehicle Technology Directorate, Cleveland, Ohio 44135

A duct was designed to transition flow from the low-pressure exhaust port of a wave rotor to the exhaust piping of a test cell. The transition duct has an annular cross-section with an inflow of 86 degrees and an outflow of 180 degrees. The geometry was generated analytically with automated grid generation for analysis using the Wind-US computational fluid dynamics (CFD) code. Design factors were examined using methods of statistical design of experiments (DoE) to obtain an optimum duct that maximized total pressure recovery and static pressure coefficient while maintaining reasonable values of outflow total pressure distortion and exit flow angularity. The duct has been fabricated and is scheduled to be tested in the NASA-Glenn Wave-Rotor Component Rig.

Nomenclature

A	=	cross-sectional area
α, β	=	flow angles
C_p	=	static pressure coefficient
DPCPAV	=	ring-average circumferential total pressure distortion
γ	=	ratio of specific heats
h	=	height
L	=	length
Ω	=	rotational speed of the wave rotor
p	=	static pressure
p_t	=	total pressure
ϕ	=	offset angle
r	=	radius
ρ	=	static density
T	=	temperature
θ	=	sector of the partial annulus cross-section
u,v,w	=	flow velocity components

I. Introduction

WAVE-ROTOR technology offers the potential to increase the performance levels of gas turbine engines. The wave-rotor component and its adaptive ducting can function as a topping cycle that effects an increase in the overall pressure ratio and the peak temperature of the cycle. This can result in increased fuel efficiency and power density and decreased emissions. The wave-rotor topping cycle has been described in detail in Ref. 1.

Figure 1 shows a schematic of a wave rotor. A tip-shrouded rotor is surrounded by a stationary casing. The casing end-walls are penetrated by inlet and exhaust ports that move gases of different pressure and temperature to and from the rotor flow-annuli. The rotor hub, tip-shroud, and blade surfaces define rotor passages. The wave-rotor passages are designed to exchange energy efficiently between gas streams of differing energy density. Gas dynamic

* Aerospace Engineer, Propulsion Systems Division, Inlet Branch, MS 86-7, AIAA Senior Member.
† Aerospace Engineer, Engine Components Division, Compressor Branch, MS 5-11, AIAA Senior Member.

(shock and expansion) waves are initiated as the rotor passages open and close in a timed sequence set by the rotor speed and azimuthal location and extent of the ports. These waves compress and expand the gas as they propagate through the rotor passages. Various gas dynamic wave cycles can be effected by the purposed tangential placement of the various ported flows. The flow exiting the wave rotor of concern in this study is subsonic, unsteady, and contains significant circumferential variation in total pressure and total temperature.

The effective use of the exhaust of a wave rotor to drive a turbine requires a transition of the flow in a manner that 1) recovers total pressure efficiently, 2) maximizes the static pressure recovery, 3) minimizes thermal, entropic, and velocity distortions, 4) "de-swirls" the flow to turn it to the axial direction, and 5) attenuates the levels of unsteadiness. To address this challenge, a study was performed to design a transition duct for the wave-rotor component rig at the NASA Glenn Research Center. This paper discusses the aerodynamic design of the duct, which has been fabricated and is scheduled to be tested in the wave-rotor component rig.

The approach for the aerodynamic design of the transition duct was to parameterize the duct geometry to yield a set of geometric design factors. Computational fluid dynamics (CFD) methods solved the Navier-Stokes equations to simulate the turbulent flow through each transition duct configuration. The aerodynamic design focused on addressing items 1 through 4 listed above. The unsteady character of the flow was not examined; rather, the time-mean flow field discharged from the wave rotor was used to set the inlet flow conditions for the design study. Methods of statistical design of experiments (DoE) were used to determine which design factors significantly affected the flow performance and to obtain an optimum design.

The challenge of designing a transition duct for the wave rotor was addressed in an earlier effort conducted at the Allison Engine Company.[2,3] They used analytical and CFD methods to design a series of three transition ducts. The current effort used their findings and started with a baseline duct that maintains key diffuser parameters of their optimum duct (Concept 1B). The Allison design included turbine nozzles near the exit of the transition duct. In the current effort, only the portion of the transition duct upstream of the nozzles is considered. The transition duct of the current study is connected to an isolator duct which is then connected to a round exhaust pipe so as to mate with the component test cell piping.

The following sections discuss the geometric modeling of the transition duct and the determination of the design factors. The grid generation and CFD methods are then discussed with an emphasis on the inflow boundary condition. The results of the CFD studies are then presented to show the progression from the baseline transition duct to an optimum duct.

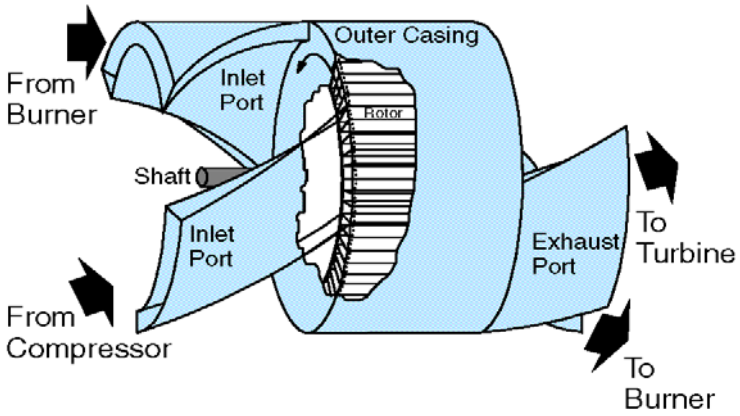

Figure 1. Four-port wave rotor schematic (Ref. 1).

II. Duct Geometry Model

The geometry model defines the transition duct with respect to a set of design factors such that the duct adheres to the specified design requirements. A baseline transition duct was established by using the effective diffuser length ratio and area schedule of the Allison Concept 1B duct of Ref. 3. An optimization with respect to the design factors was then performed to obtain the final duct.

A. Design Requirements

The design requirements were:

1) The transition duct will transition the flow path from the partial annular shape of the low-pressure exhaust port (exhaust port 4 to turbine of Fig. 1) with an opening of 86.07 degrees to a partial annular shape with an opening of 180.0 degrees. Figure 2 shows a transition duct.
2) The inflow to the transition duct should match the partial annular shape and internal surface angles of the low-pressure exhaust port in the exit end plate of the wave rotor.
3) The flow-path walls of the transition duct inlet must be tangent to the walls of low-pressure exhaust port for 30% of the duct length. This requirement assumes that a constant area section at the start of the diffuser allows some distance for the circumferential variations to mix, and so, dissipate.
4) The outflow of the transition duct should be directed axially and be a partial annulus with a height of 1.3 inches, which equals the height of the inflow.
5) The normalized distribution of the cross-sectional area of the baseline duct should match that of the Concept 1B duct of Ref. 3.
6) The length of the transition duct will be scaled to that of Concept 1B of Ref. 3, as described in section D.
7) The transition duct will connect to an isolator that will have a constant partial annulus cross-section matching that of the transition duct exit (180 degrees). Figure 2 shows the isolator.
8) The isolator will connect to a coupler that will transition from the 180 degree partial annular opening of the isolator to a circular opening of the exhaust pipe, which can be connected to the existing test cell pipes. Figure 2 shows the coupler with a small section of the exhaust pipe.
9) The total length of the transition duct, isolator, and coupler should reasonably fit within the space constraints between the wave-rotor and exhaust pipes.
10) The outer surface of the case should not interfere significantly with the motor or other test rig hardware.

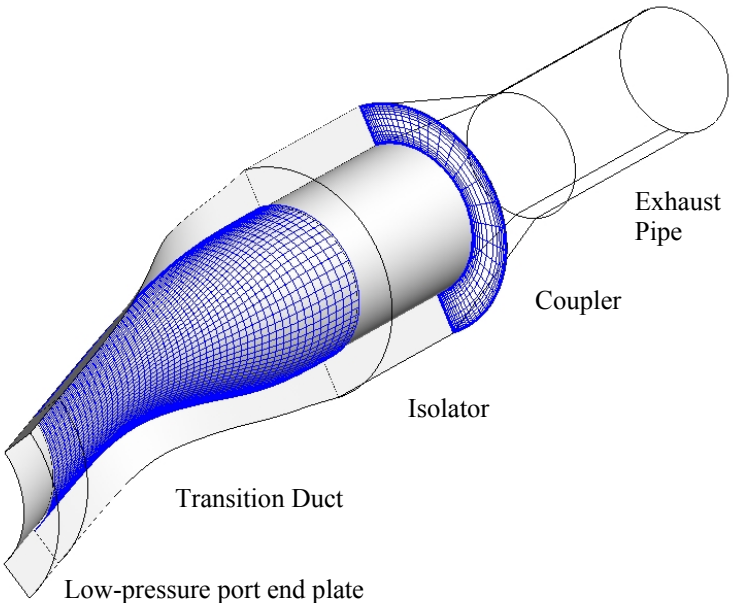

Figure 2. Flow domain, geometry, and grid for the baseline transition duct.

B. Cross-Section Shape

The cross section of the transition duct is a partial annulus defined by two arcs and two radial lines and can be defined at each axial station along the duct. Figure 3 shows the cross-sectional plane as looking down the x-axis (downstream). The coordinate system for the model is a Cartesian system with the x-coordinate in the axial direction. The coordinate system has its origin at the center of radius of the low-pressure exhaust port. The hub and

case are defined by the hub and case radii r_H and r_C, respectively, and the annular extent θ. The angular offset of the trailing wall is ϕ. The area of the cross-section is

$$A = \frac{1}{2}\theta\left(r_C^2 - r_H^2\right) \tag{1}$$

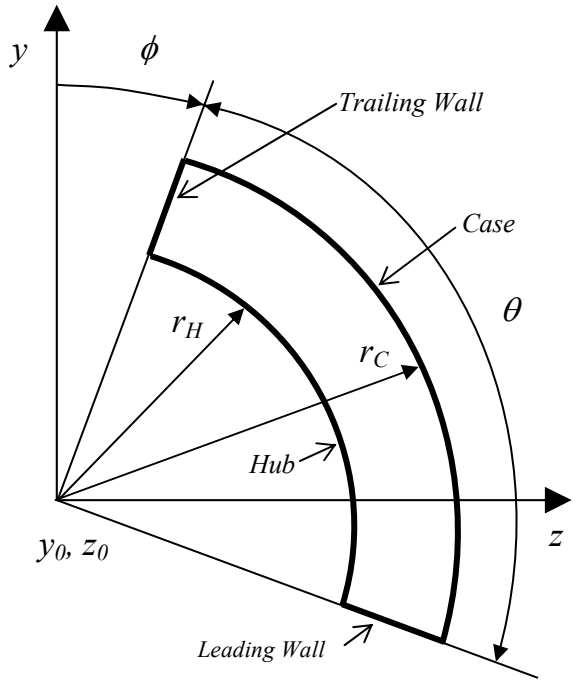

Figure 3. The partial annulus cross-section at an axial station of the transition duct. The view is looking downstream in a right-hand coordinate system.

C. Wave-Rotor Exhaust Port Geometry

The inflow of the transition duct connects to the low-pressure exhaust port of the wave rotor (see Fig. 1). The port outflow is a partial annulus and follows the cross-section model shown in Fig. 3 with r_H = 2.7 inches, r_C = 4.0 inches, θ_{inflow} is 86.07 degrees, and ϕ_{inflow} = 52.62 degrees. The internal shape of the port walls have a slight s-shape; however, they were approximated to be flat surfaces with a circumferential angle of -17.1 degrees. The radial angles varied across the circumference of the port. At the leading wall, the radial flow angle was -16.0 degrees. At the trailing wall, the radial flow angle was 15.9 degrees. The start of the transition duct was required to match these angles.

D. Duct Length

The length of the transition duct was a determined by scaling the length of the Allison Concept 1B duct of Ref. 2 using the relation

$$L_{duct} = \left[\left(\bar{r}\,\theta\right)_{in}\right]_{baseline}\left[\frac{L}{\left(\bar{r}\,\theta\right)_{in}}\right]_{Allison} . \tag{2}$$

Table 1 lists the properties of the Concept 1B and baseline transition ducts. Using these properties and Eqn. 2, the length of the transition duct was computed to be L_{duct} = 16.267 inches, which was then fixed for the design studies. The duct length could have been a design factor. A longer duct can provide a greater distance for static pressure recovery; however, a shorter duct translates into weight savings in application. Fixing the duct length based on the scaling of the Concept 1B duct implied that the design of the Allison duct considered these two competing aspects.

Table 1. Properties of the Allison Concept 1B and Baseline ducts.

Duct	Allison Concept 1B	Baseline
$(y_0, z_0)_{inflow}$	(0.0, 0.0) in	(0.0, 0.0) in
$r_{H\ inflow}$	2.711 in	2.7 in
$r_{C\ inflow}$	3.641 in	4.0 in
$\bar{r}_{inflow}$	3.21 in	3.41 in
ϕ_{inflow}	45.0 deg	52.6195 deg
θ_{inflow}	45.0 deg	86.0691 deg
A_{inflow}	2.320 in^2	6.5420 in^2
L_{duct}	8.0 in	16.267 in
$(y_0, z_0)_{outflow}$	(0.0, 0.0) in	(0.0, 0.0) in
$r_{H\ outflow}$	2.6 in	2.4413 in
$r_{C\ outflow}$	3.1 in	3.7414 in
$\phi_{outflow}$	-62.84 deg	-22.41 deg
$\theta_{outflow}$	180.0 deg	180.0 deg
$A_{outflow}$	4.477 in^2	12.6261 in^2
$L_{isolator}$	-	6.0 in
$L_{coupler}$	-	6.0 in
r_{Cex}	-	2.013 in

E. Transition Duct Outflow

The outflow is specified to have a sector angle of $\theta_{outflow}$ = 180.0 degrees. It should be noted that the Allison Concept 1B duct also had an outflow sector angle of 180 degrees; however, the exhaust port sector angle was 45 degrees, whereas the current duct as an exhaust port sector angle of 86.1 degrees. Thus, the Allison duct involves a more extreme circumferential opening of the flow. The rapid circumferential opening was offset by a decrease in duct height, ultimately setting the area schedule shown in Fig. 4. Further, the flow is specified to be directed axially. The center of radius (y_0, z_0), hub radius (r_H), case radius (r_C), and the off-set angle (ϕ) are not directly specified, and so, will be determined as part of the design process. The circumferential offset angle ϕ of the outflow for the baseline duct is computed from a scaling of the circumferential angles of the Concept 1B duct using the relation

$$\phi_{outflow} = \phi_{\inf low} + \left[\frac{\phi_{outflow} - \phi_{\inf low}}{\theta_{outflow} - \theta_{\inf low}}\right]_{Allison} \left(\theta_{outflow} - \theta_{\inf low}\right)_{Baseline} \tag{3}$$

This results in an outflow off-set angle of $\phi_{outflow}$ = -22.41 degrees.

F. Cross-Sectional Area Distribution

A design requirement for the transition duct was that the normalized distribution of the cross-sectional area had to match that of the Concept 1B duct of Ref. 3. The area variation is normalized as A / A_{inflow}. The Concept 1B duct had an inflow area of A_{inflow} = 2.320 in^2 and an outflow area of $A_{outflow}$ = 4.477 in^2. This resulted in a duct area ratio of $A_{outflow} / A_{inflow}$ = 1.930. From Table 1, the inflow area of the baseline duct is constrained to be A_{inflow} = 6.542 in^2. Using the same duct area ratio as the Concept 1B duct, the outflow area for the baseline duct should be $A_{outflow}$ = 12.625 in^2. Figure 4 shows the variation of the normalized cross-sectional area of the Concept 1B duct. The variation of the area with respect to the axial coordinate x was modeled using a non-uniform rational B-spline (NURBS) curve with 8 control points, which are plotted in Fig. 4. The NURBS curve allowed the tangency to be set at the ends of the curve while allowing local control of the shape of the curve according to the location of the control points. Another requirement was that flow path walls were to be tangent to the walls of low-pressure exhaust port for approximately 30% of the transition duct length. This was implemented by specifying that the slope of the control polygon at the start of the curve would have a zero slope, which resulted in the first three control points having a normalized area of 1.0. The NURBS curve matches the position of the first control point, and matches the slope of the two control points at its end. At the end of the area variation, there is a distinct slope. This is matched by the control polygon by placing the last three control points to be along a line with the slope matching that of the

area variation. The area variation of the Concept 1B duct sort of "levels-off" a bit between x / L of 0.45 and 0.65. To model this, the two interior control points of the NURBS curve we set to be the same area ratio. The resulting area variation is shown in Fig. 4 (dashed curve) and it closely matches that of the Concept 1B duct (solid curve).

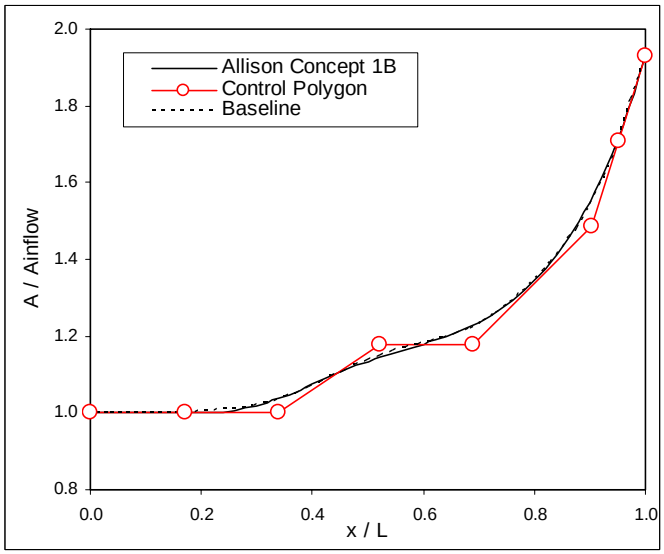

Figure 4. NURBS variation of the scaled duct cross-sectional area.

G. Transition Duct Surface Design

The flow surfaces of the transition duct include the leading and trailing walls and then hub and case surfaces. At axial stations, these surfaces combine to form the cross-section model shown in Fig. 3. Requirement 2 above indicated that the angles of the surfaces of the transition duct at the inflow should match the angles of the internal surfaces of the wave rotor low-pressure exhaust port. To match these angles, three (3) three-dimensional NURBS curves with six (6) control points each were generated to define the hub surface of the transition duct. The curves have endpoints at the inflow and outflow sections. Two curves define the corners of the hub surface with the leading and trailing walls, respectively. The third curve defines the axial shape of the hub surface at the mid-circumferential location. The angles of the internal surfaces of the wave rotor low-pressure exhaust port are matched by matching the angles of the respective NURBS curve at the inflow. Requirement 4 indicated that the duct outflow should be directed axially. This was met by specifying the angles of the three NURBS curves to be directed axially. The three NURBS curves along the hub surface allow three points to be defined at each axial station between the inflow and outflow planes. These three points define the arc needed for the cross-section as shown in Fig. 3. This further allowed the hub radius (r_H) and center point (y_0, z_0) of the cross-section to be defined using an iterative procedure. This resulted in an axial variation of the center-point, which resulted in the duct cross-sections not being co-axial.

The offset angle ϕ is the angle between the local y-axis of the cross-section and the line defining the trailing wall. The sector angle θ was determined from the angle of the arc between NURBS curves defining the trailing and leading edges of the hub, respectively. Using the specified area variation, the case radius is computed from

$$r_C = \sqrt{r_H^2 + \frac{2A}{\theta}} \,. \tag{4}$$

H. Isolator

The purpose of the isolator duct is to isolate the transition duct from the flow effects of the coupler. The isolator duct is a constant-area, straight duct co-axial with the cross-sectional properties the same as the outflow cross-section of the transition duct. The length of the isolator duct $L_{isolator}$ was set to have a length of $L_{isolator}$ = 6.0 inches.

I. Coupler

The coupler transitions the flow path from the half-annulus cross-sectional shape of the isolator to the circular cross-section of the pipe of the exhaust system for the test rig. The inflow and outflow cross-sections are co-axial. The cross-sectional area through the coupler monotonically decreases, which makes the coupler a nozzle. From preliminary CFD simulations, it was determined that a length of $L_{coupler} = 6.0$ provided an acceptable distance for the flow to transition while keeping the length to a minimum. The shape of the duct was initially defined by generating four NURBS curves that start at the respective corners of the half-annulus section and end at the round cross-section. The spacing of the end-points around the round cross-section was in the same ratio as the spacing of corners around the half-annulus section. The slopes of the NURBS curves at the start and endpoints were directed axially. The shape of the surfaces between the curves was generated using a transfinite interpolation, which is performed during the grid generation using GRIDGEN. This generated surfaces with an s-shape as shown on the left-hand side of Fig. 5. It was determined during the mechanical design that the coupler could be fabricated quicker and with less cost using a hot-wire cutting method rather than surface machining. This required the corners of the coupler to be straight lines rather NURBS curves. This simpler model is shown on the right-hand side of Fig. 5. CFD simulations of the flow through both designs indicated minimal adverse effects. Thus, the straight-line model was used for the coupler.

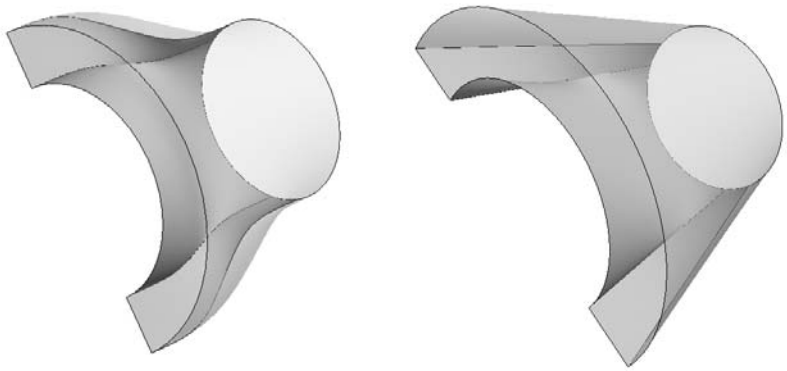

(a) **(b)**

Figure 5. Coupler designs: (a) s-shaped and (b) straight.

J. Design Factors

The design factors for the transition duct are summarized in Table 2 in terms of the geometry model, constraints, and requirements. While experience may provide some insight as to the effect of the factors on the performance of the duct, formally, the exact effect is unknown *a priori*. There also exist the possibilities of interactions between the factors that further complicate optimizing the design. The approach for sorting out the effect of each factor and their interactions is to use statistical methods of Design of experiments (DoE). That approach will be expanded upon in a later section.

Table 2. Design factors for the transition duct.

Design Parameters	Design Factors	Number
Off-set at the outflow	$\phi_{outflow}$	1
Inflow angles of sidewalls	α_{inL}, $D_{\alpha inL}$, α_{inT}, $D_{\alpha inT}$	4
Radial angles of hub	dr/dx_T, dr/dx_L	2
Outflow angles of sidewalls	α_{outL}, $D_{\alpha outL}$, α_{outT}, $D_{\alpha outT}$	4
Area *A* variation	dA/dx_in, D_{Ain}, dA/dx_out, D_{Aout}, A_{45}, x_4, x_5	7
	Total	18

K. Computational Flow Domain

The computational flow domain defines the volume in which the flow field is simulated. Figure 2 shows the flow domain used in the simulations. From the inflow to the outflow, the flow domain consists of the low-pressure exhaust port end plate, transition duct, isolator, coupler, and then a short segment of the exhaust pipe.

III. Grid Generation

A CFD simulation requires a multi-zone, structured grid to be generated for the duct geometry and flow domain. The Fortran 90 program WTDUCT was written to efficiently generate the geometry and grid. Figure 6 shows the contents of a typical design input file.

```
Wave Rotor Transistion Duct
Design 0: Constant-height   1: Theta based on curves.
             1
 r1_in     r2_in     Phi_in    Theta_in
  2.7       4.0       52.6195     86.0691
 r1_out   A_ratio    Phi_out   Theta_out   y0_out   z0_out
 2.4413     1.930    -22.41       180.0      0.0      0.0
 Lduct     dxin     dxex    dxmax    ni   niso   liso
 16.267     0.2      0.4      0.4    51     15    6.0
dswall     delta    sref    dsref    nj     nk   ngbl
 0.000423  0.234   5.8768     0.3    75    155     29
Area NURBS:  dAdx_in DA_in dAdx_out DA_out Area45 Xarea4 Xarea5
               0.0     5.53    1.85   3.3    7.72  8.459  11.224
Inflow End-Walls:  alpha_T  Dalpha_T   alpha_L  Dalpha_L
                    -17.1      5.53     -17.1      5.53
Hub Inflow Slope:   drdx_T    drdx_L
                     15.9     -16.0
Outflow End-Walls: alpha_T  Dalpha_T   alpha_L  Dalpha_L
                      0.0       3.3       0.0       3.3
Round.    L_C      r_rnd   y0_rnd  z0_rnd   ni_rnd
          6.0      2.013     0.0     0.0      15
Round Extension.  L_rex   ni_rex   ni_endplate
                   8.0       19        9
```

Figure 6. Input file to WTDUCT for the baseline duct.

The grid was generated using specific grid quality parameters to ensure a quality grid capable of resolving the important features of the flow. The grid quality parameters drive the generation of the grid and determine the number of grid points to resolve the flow. Primary among the flow features to be resolved are the turbulent boundary layers along the surfaces of the duct. Critical is the resolution of the flow gradients through the boundary layer in a direction normal to the duct surfaces. The grid quality parameters for the grid through the boundary layer is the spacing of the first grid point off the wall (dswall) and the grid spacing ratio (r_g). The grid spacing at the wall is related to the non-dimensional distance y^+ for a turbulent boundary layer. The proper resolution of a turbulent boundary layer, especially one that might separate, is typically less than $y^+ = 1$. Grids with coarser resolution can be generated using y^+ values of 2 and 5. The grids generated in this work used values of $y^+ = 1$ for the fine and medium grids and $y^+ = 2$ for the coarse grid. The grid spacing that would result approximately in those values of y^+ was determined from preliminary CFD simulations of the baseline duct. From examining the boundary layer at several locations within the duct, it was determined that a wall spacing of dswall = 0.0005 inches resulted in a y^+ value of approximately 3.0. The value of y^+ is known to vary approximately linearly for values of y^+ below about 50. Thus, a simple ratio determined that a value of $y^+ = 1$ could be obtained with dswall = 0.00017 inches. A value of $y^+ = 2$ could be obtained with dswall = 0.00034 inches. The grid spacing ratio, r_g, is defined as the ratio of the spacing of adjacent grid points along the grid line such that the ratio is equal or greater than one. A good value is between 1.15 and 1.2. Coarser grids can approach values of 1.3. The grids generated here used a maximum grid spacing ratio of $r_g = 1.2$.

In the axial or streamwise direction, the grid quality parameters were the axial grid spacing at the inflow (dxin) and exit (dxex) of the transition duct. There can also be a maximum axial grid spacing (dxmax) specified; however, this was assumed to be equal to the value of dxex. The stretching of the grid in the axial direction was kept below a maximum value set by the grid spacing ratio of $r_g = 1.2$.

In the radial direction, boundary layers existed at the hub and case and the grid quality parameters defining the resolution through a boundary layer, as already discussed, were applied. In the core of the flow between the boundary layers, the maximum grid spacing ratio of 1.2 was maintained. A maximum radial grid spacing (drmax) could have been specified with a value similar to the maximum axial or circumferential grid spacing. However,

because the height of the duct was much smaller than the length or circumference of the duct, the radial grid spacing never approached those values and did not become an issue.

In the circumferential direction, boundary layers existed at the leading and trailing walls and the grid quality parameters defining the resolution through a boundary layer, as already discussed, were applied. In the core of the flow between the boundary layers, the maximum grid spacing ratio of 1.2 was maintained and a maximum circumferential grid spacing (dsmax) was specified.

The grids in the transition duct and the isolator were generated as planar grids at a constant-x station. The grid points were distributed along the curves of the planar section outlining the surfaces of the ducts. A transfinite interpolation was then applied to generate the interior grid on the plane. Figure 6 shows an example of the grid.

IV. Performance Measures

The performance measures of the transition duct included 1) the total pressure recovery, 2) the static pressure coefficient, 3) the circumferential total pressure distortion of the outflow, and 4) circumferential angle of the outflow.

The *total pressure recovery* measures the loss of flow energy through the transition duct, and so it should be maximized. The total pressure recovery is computed as the ratio of the mass-averaged total pressures of the outflow and inflow to the transition duct,

$$\text{Recovery} = \frac{p_{t_{outflow}}}{p_{t_{\text{inf}low}}}. \tag{5}$$

The *static pressure coefficient* measures the amount of diffusion (compression) that occurs within the transition duct. The objective is to maximize the pressure coefficient. The pressure coefficient is computed as

$$C_p = \frac{2(p_2 - p_1)}{\rho_1 V_1^2}, \tag{6}$$

where p_1 and p_2 are the area-averaged static pressures at the inflow and outflow, respectively. The ρ_1 and V1 are the static density and velocity magnitude of the inflow.

The *circumferential total pressure distortion* of the transition duct outflow measures the spatial variation of the total pressure. A high level of distortion may cause flow problems with downstream devices, especially rotating turbomachinery, and so, the objective is to reduce distortion to below an acceptable level. The methods of SAE ARP 1420 are used to compute the distortion descriptor DPCPAV[4]. The total pressure at the outflow is first interpolated onto a polar rake in which its probe locations are area-weighted. A standard 40-probe rake has 5 rings and 8 rakes for a 360-degree circular outflow. For the 180-degree outflow of the computational flow domain, a rake with 17 rings and 65 rakes was used to ensure a high resolution of the total pressure variation. The program CFPOST was used to perform the interpolation and compute the SAE ARP 1420 circumferential distortion intensity element ΔPC/P for each ring. An algebraic average of the ΔPC/P values of the rings yielded the descriptor DPCPAV.

The *circumferential angle of the outflow* of the transition duct measures how the flow is directed. The objective is to have both the local and average flow directed axially. The Fortran 90 program circum performed a mass-average along each radial grid line to obtain a circumferential variation of the flow angle. This circumferential variation was then average to get an overall average outflow angle.

V. CFD Methods

The flow fields for the transition ducts were simulated using the Wind-US CFD code[5]. Wind-US is being developed by the NPARC Alliance (National Program for Applications-oriented Research in CFD), which is an alliance of the NASA-GRC, the U.S. Air Force Arnold Engineering Development Center, and the Boeing Company. Wind-US solves the Reynolds-averaged Navier-Stokes equations in a time-dependent manner for turbulent, compressible flows using a cell-vertex, finite-volume, time-marching approach. Spatial accuracy is formally second-order using the Roe flux-difference splitting upwind formulation. Wind-US is capable of solving for flows of speeds ranging from low subsonic to hypersonic. Wind-US can compute unsteady or steady flows. Unsteady flows can be computed implicitly or explicitly using second-order time-accurate methods. Steady flows are simulated through a first-order, implicit Euler method that iterates using local time stepping based on a global CFD

number. Turbulence was modeled using the one-equation Spalart-Allmaras or the two-equation SST eddy viscosity models. The conditions on the boundary of the flow domain are required to be specified. The boundaries can be grouped into the duct surfaces, inflow, and outflow boundary. The following sections discuss how the boundary conditions were applied.

A. Duct Surfaces

The surfaces of the end plate, transition duct, isolator, coupler, and exhaust pipe are all solid surfaces with no flow through them. The flow adheres to the surface to create a no-slip condition that results in boundary layers forming on the surfaces. Those boundary layers are assumed to be turbulent. The surfaces are also assumed to be adiabatic, which indicates no thermal energy is transferred through the surfaces.

B. Inflow

The inflow boundary of the computational flow domain takes inflow set by the time-average of the flow discharged from the wave-rotor passages. The wave rotor rotates at a constant rotational speed of Ω = - 10500 rpm. The negative sign indicates that the rotation is opposite of the right-hand rule (thumb down the axis and fingers wrapped around the x-axis in the direction of positive rotation). As the wave rotor rotates, each wave rotor channel is exposed to the lower pressure of the low pressure exhaust port and transition duct, and so, expansion waves enter the wave rotor and expel the passage contents. The pressure and velocities of the flow are greatest at the leading wall of the transition duct. The non-uniform wave-rotor passage contents and the expansion wave create a circumferential variation in the total pressure and total temperature at the inflow. The flow discharged from the rotor into the exhaust port is actually highly unsteady; however, the time-mean of the rotor discharge is used to set the inflow conditions in the design study. Thus, the CFD simulations used for the design of the transition duct assumed a steady-state inflow and the simulations assume convergence to a steady-state flow field.

The inflow from the wave rotor remains subsonic, and so, the boundary condition requires four physical conditions and one numerical condition. The numerical condition is obtained through extrapolation of some flow property (such as the Riemann invariant) from the interior of the flow domain. The four physical conditions where chosen to be the total pressure, total temperature, circumferential velocity, and the condition of radial equilibrium. The next few paragraphs will discuss each of these in detail.

The circumferential variations in total pressure and total temperature were determined from simulations of the wave rotor flow using a quasi-one-dimensional CFD code[6]. Figure 7 shows these variations in the total pressure and total temperature across the circumference of the inflow.

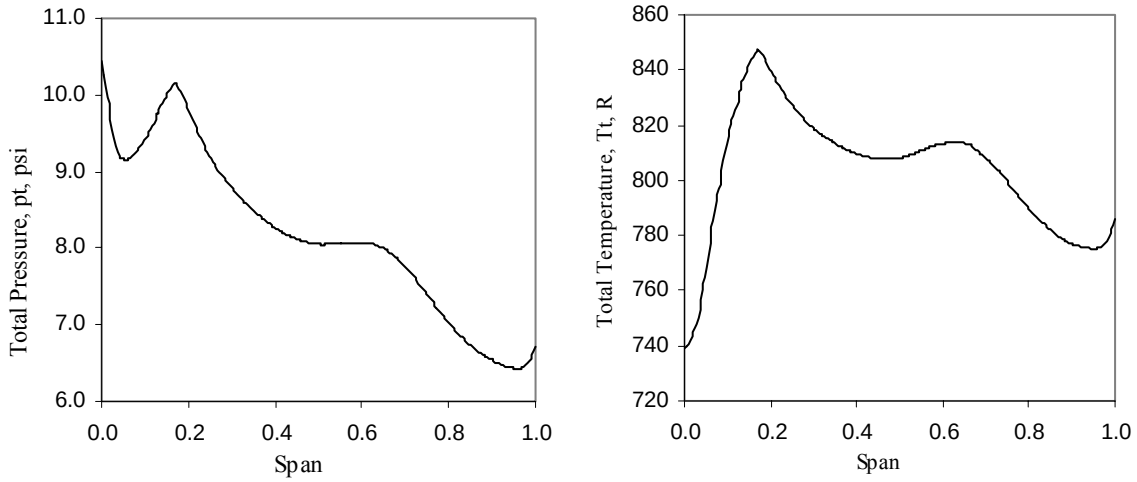

Figure 7. Circumferential total pressure and total temperature profiles at duct inflow.

The third physical condition of the inflow is that the tangential velocity component is equal to the rotation of the wave rotor

$$u_\theta = r\,\Omega\,. \tag{7}$$

The final physical condition is that of radial equilibrium, with the assumption of a zero radial velocity ($u_r = 0$). The inputs to Wind-US are in the Cartesian frame of reference. The velocity components are transformed between the cylindrical frame (x,r,θ) and Cartesian (x,y,z) frame with the following expressions

$$\begin{aligned} v &= -u_\theta \sin\phi \\ w &= u_\theta \cos\phi \end{aligned} \tag{8}$$

where ϕ is the circumferential angle from the y-axis in the y-z plane. The inflow boundary condition in Wind-US requires the local flow angles to be determined, which are computed from the velocity as

$$\begin{aligned} \alpha_{xyz} &= \tan^{-1}\left(\frac{v}{u}\right) \\ \beta_{xyz} &= \tan^{-1}\left(\frac{w}{u}\right) \end{aligned} \tag{9}$$

The condition of radial equilibrium also results in a radial variation of the total pressure and total temperature. The circumferential variations of total pressure and total temperature shown in Fig. 7 are assumed to be located at an average radial distance of

$$\bar{r} = \frac{1}{2}\left(r_H + r_C\right). \tag{10}$$

We define the radial variations in the total pressure and total temperature as

$$p_t(r,\theta) = p_t(\bar{r},\theta)\,\Gamma^{\gamma/(\gamma-1)} \tag{11}$$

and

$$T_t(r,\theta) = T_t(\bar{r},\theta)\,\Gamma \tag{12}$$

where

$$\Gamma = 1 + \frac{(\Omega\,\bar{r})^2}{h_t(\bar{r},\theta)}\left[\left(\frac{r}{\bar{r}}\right)^2 - 1\right] \tag{13}$$

and

$$h_t = \frac{\gamma R T_t}{\gamma - 1}. \tag{14}$$

The values of Γ at the hub and tip at the mid-radius were calculated to be $\Gamma_{hub} = 0.9931$ and $\Gamma_{tip} = 1.0083$. This seems to suggest that there was not a strong radial variation for the total pressure and total temperature.

In applying this boundary condition, the "arbitrary inflow" boundary condition of Wind-US was used to specify the conditions at the inflow boundary. The "hold_totals" option was used which allowed the specification of the total pressure, total temperature, and local flow angles for the grid points on the inflow boundary. The "ijk_range" option was used to specify the circumferential total pressure and total temperature variations as shown in Fig. 7 at the mid-radius. Wind-US was modified to impose the tangential velocity and the condition of radial equilibrium.

C. Outflow

The transition duct exhausts flow to the isolator and coupler which is then attached to the exhaust pipe of the test rig. The flow is subsonic as it exits through the exhaust pipe. The computational flow domain includes a short length of the exhaust pipe. Placing the outflow boundary several duct diameters downstream of the transition duct assures that the flow field in the transition duct is not sensitive to the CFD boundary condition applied at the outflow boundary. For the CFD simulations, the weight flow in lbm/sec was specified at the outflow boundary. This boundary condition essentially adjusted the static pressure on the outflow boundary until the actual weight flow matched the specified value.

D. Iterative Convergence

Iterative convergence was determined by monitoring the variations of the total pressure recovery, pressure coefficient, and Mach number at the exit of the transition duct and the variations of the mass flow through the duct. Iterative convergence was considered reached when these changes over a large number of iterations are below a approximately one percent. The converged flow field was not dependent on the initial flow field, so the initial flow field was established as a uniform flow using a guess of the average Mach number, total pressure, and total temperature of the duct flow. The iterative nature of the simulation and the boundary conditions determined the final flow field.

VI. CFD Studies

CFD studies were performed first to examine the baseline duct and explore accuracy issues related to turbulence modeling, grid density, and zone coupling for transition duct simulations. The next study used methods of statistical design of experiments (DoE) to examine some of the design factors presented in Table 2 and determine which factor was most significant. A final design study optimized the transition duct performance for the significant design factors.

A. Baseline Duct

A CFD study was performed for baseline transition duct described by Table 1. The results provided a baseline aerodynamic performance. To examine accuracy issues with regard to turbulence modeling, grid density, and zone coupling, a series of simulations were performed. This study was performed before the decision to use the inflow boundary conditions as detailed in section V. Rather, the total pressure and total temperature profiles of Ref. 2 were used after scaling them to the wave-rotor rig conditions. More importantly, the inflow angles were specified to be aligned with the inflow grid lines, which were aligned with the angles of the surfaces. The outflow weight flow was 0.75 lbm/sec. It was felt that the general conclusions of this study with respect to grid density and turbulence model sensitivities still applied to later simulations with the inflow boundary conditions as detailed in section V.

A grid convergence study examined the variation of the performance measures to grid density and quality. As the grid is refined and the quality improved, the variation should reduce and the value of the performance measures should approach a fixed value. In practice, some variation is accepted due to limited computational resources, which increase as the grid is refined. A grid convergence study helped define the acceptable variation with respect to the computational resources. For the grid convergence study of the baseline duct, three grids of various densities (coarse, medium, and fine) were generated. Table 3 lists the grid quality parameters and values used in generating a coarse, medium, and fine grids used for the grid convergence study. In turn, each of these grids could be run using grid sequencing to perform the solution on every other grid point in each coordinate direction. Grid convergence is examined by simulating the flow field on successively finer grids and observing the variation in the performance measures. Table 4 lists the performance measures for the various grids and Fig. 8 plots the values. The Mach number listed in the table is the mass-averaged Mach number at the transition duct outflow. No clear trend was apparent between the performance measures with respect to grid density. The conclusion was that the medium grid seemed to be adequate to resolve the flow.

One assumption of the flow field was that it was fully turbulent. The choice of turbulence model may affect the values of the performance measures. To examine possible variation due to choice of turbulence model, CFD simulations were run with the Spalart-Allmaras and the SST models. These two models are the two choice models for flows with adverse pressure gradients and possible boundary layer separation. A simulation was attempted with the Baldwin-Lomax model; however, it became apparent by large separation regions and poor iterative convergence that the Baldwin-Lomax model was not an appropriate choice for this flow field. There were significant variations in the performance measures due to turbulence model. Without further guidance on which model might be better, the Spalart-Allmaras model was chosen for subsequent simulations. The approach was that for the consistent comparison of flow fields, one should stick to one model. Simulation BFf was run using the wall function with the S-A turbulence model. In comparison to simulation BFe, there was significant variation (2.4%) in the pressure coefficient. While the use of the wall function might reduce the wall-clock time required for the computations, it was decided to use the full grid and integrate the turbulence equations to the wall. The presence of separated boundary layers and adverse pressure gradients also suggested that use of the wall function was not advised.

The flow domain is divided into zones and grid is defined within each zone. This allows a structured grid to be more easily generated for a complex flow domain and reduces the amount of computer memory needed for the simulation. During a simulation, each zone is loaded into memory and assigned a processor. Iterations on the

governing equations occur within each zone. Information is then transferred between the zones at the boundaries of the zones. The flow domain of this work is fairly simple and can be modeled with a single-zone. Dividing the flow domain into up to 15 zones allows fast wall clock processing on multi-processor computers. The cfcombine and cfsplit utilities were used to combine and split the grids into the number of desired zones for each simulation. Simulations were run for various zonal combinations. While Wind-US transfers inviscid information across zonal boundaries in an accurate manner, the turbulent properties are transferred using a simple interpolation. The flow field of this work shows significant gradients in the flow and some smaller regions of low-energy and separating flow. Thus, this case provides a good case to examine zonal coupling issues. One issue is whether dividing the grid into 15 zones will cause a significant variation in the values of the performance measures. The simulations BFe, BFb, and BFd all impose the same conditions, except that 2, 4, and 15 zones are used, respectively. There is significant variation in the values of the performance measures which suggests that the values are sensitive to the presence of zonal boundaries. The variations do not seem to be consistent. One would think that having the least number of zonal boundaries would result in the least error. The conclusion of this study is one should minimize the number of zonal boundaries in critical flow regions (i.e. separated regions) and if comparisons are made between performance measures, then the zonal boundaries should be the similar.

Upon completion of the grid resolution study, the resolution of the boundary layer was examined. An average y^+ of the first point off the surfaces was determined to be approximately 0.4 with a boundary layer thickness of 0.234 inches. Thus, it was felt that the wall grid spacing was too small and could be increased. Using a linear scaling of grid spacing and y^+, a new value of wall spacing was computed to be dswall = 0.000423 inches. This wall spacing was used for all subsequent CFD simulations.

Table 3. Grid Quality Parameters and values for the grid resolution study.

Grid Quality Parameter	Coarse	Medium	Fine
y^+	2	1	1
dswall	0.00034 in	0.00017 in	0.00017 in
r_g, grid spacing ratio	1.2	1.2	1.2
dxin	0.2 in	0.2 in	0.2 in
dxex	0.6 in	0.4 in	0.3 in
dsmax	0.6 in	0.4 in	0.3 in
ni	49	65	83
nj	75	83	83
nk	105	117	125
N_{duct}	385875	631215	861125
r, grid refinement ratio	1.39	1.16	-

Table 4. CFD simulation results of the baseline geometry.

Sim	Grid	r*	Zones	Turbulence	Recovery	Cp	DPCPAV	Mach
BCa	Coarse (111)	3.22	4	S-A	0.9691	0.5097	0.0245	0.1864
BCb	Coarse (000)	1.61	4	S-A	0.9676	0.5066	0.0296	0.1861
BCc	Coarse (000)	1.61	4	S-A	0.9673	0.5042	0.0297	0.1867
BCd	Coarse (000)	1.61	4	SST	0.9630	0.4434	0.0307	0.1983
BMa	Medium(111)	2.32	4	S-A	0.9687	0.4954	0.0263	0.1899
BMb	Medium(000)	1.16	4	S-A	0.9639	0.4514	0.0314	0.1994
BMc	Medium(000)	1.16	4	SST	0.9616	0.4233	0.0316	0.2024
BFa	Fine (111)	2.00	4	S-A	0.9695	0.5205	0.0265	0.1816
BFb	Fine (000)	1.00	4	S-A	0.9668	0.5029	0.0307	0.1829
BFc	Fine (000)	1.00	4	SST	0.9611	0.4190	0.0323	0.1997
BFd	Fine (000)	1.00	15	S-A	0.9665	0.4967	0.0315	0.1846
BFe	Fine (000)	1.00	2	S-A	0.9644	0.4607	0.0320	0.1965
BFf	Fine (000)	1.00	2	S-A (wf)	0.9655	0.4719	0.0307	0.1967

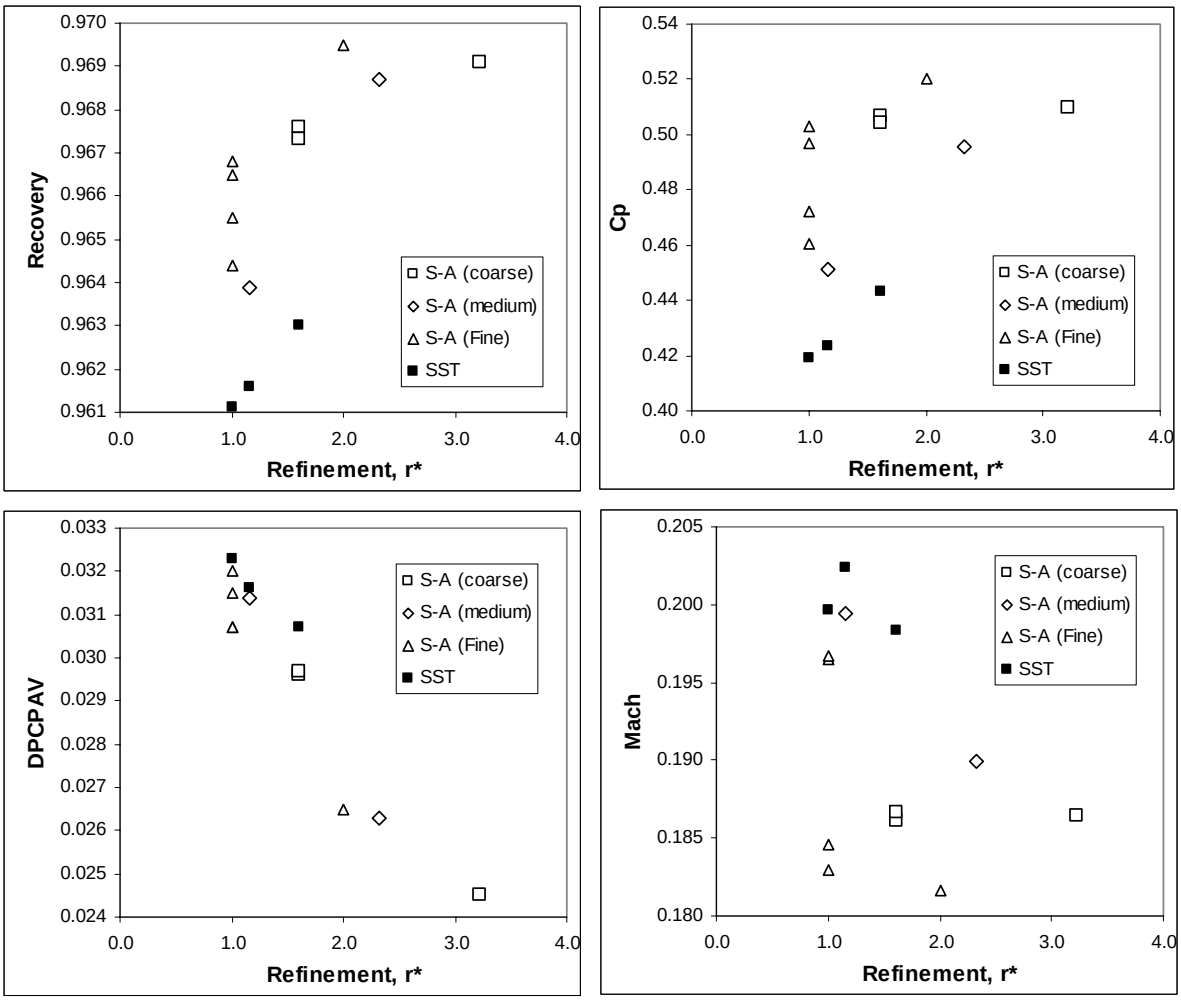

Figure 8. Performance measures from CFD simulations using various grid densities, turbulence models, and number of zones.

B. Design of Experiments (DoE) Study

The optimum transition duct is one that maximizes total pressure recovery and static pressure coefficient while keeping total pressure distortion below limits. Table 2 listed 18 geometric design factors that affect these performance measures. Finding the optimum duct requires understanding the significance of these factors and finding the values of these factors that result in the optimum performance. The list of design factors was first reduced by applying some of the constraints imposed by the design requirements. Requirement 2 constrains the duct such that the inflow angles of the sidewalls, hub, and case should match that of the low-pressure exhaust port surfaces. This sets the values for α_{inL}, α_{inT}, dr/dx_T, and dr/dx_L. A simplification was made such that $D_{\alpha inL} = D_{\alpha inT} = D_{Ain}$ and $D_{\alpha outL} = D_{\alpha outT} = D_{Aout}$. These simplifications coupled the sidewall angle variation with the area variation, which was a reasonable approximation. The area variation has an effect on the performance; however, requirement 5 constrained the area variation, and so, the seven factors for the area variation were eliminated. Requirement 3 indicated that the area should be constant for about the first 30% of the duct length, which fixed the values of dA/*dx_in* and D_{Ain}. The remaining set of design factors consisted of $\phi_{outflow}$, α_{outL}, and α_{outT} .

To examine the significance of these three design factors on the performance of the transition duct and obtain an optimum design for the transition duct, we turned to statistical methods of the design of experiments (DoE) and response surface methods (RSM)[7]. A central composite face-centered (CCF) design was used to statistically examine these factors. Figure 9 shows a diagram of the CCF design. The black circles indicate the normalized values of the design factors that were simulated. The statistical design requires 15 evaluations of the response

variable. This requires 15 CFD simulations of the various duct configurations. Table 5 lists the sets of design factors for the 15 CFD simulations. The CFD simulations were performed using the same inflow boundary condition as used for the CFD simulations of the baseline duct reported in the previous subsection, which used the total pressure and total temperature profiles of Ref. 3 and used inflow angles aligned with the inflow surfaces rather than the conditions of Section V.B.

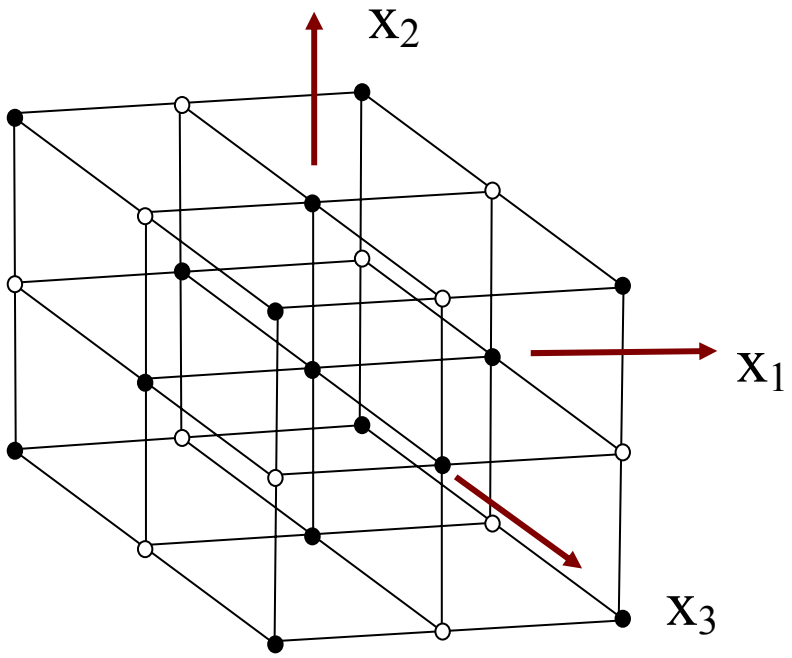

Figure 9. Central Composite Face – Centered (CCF) DoE Design.

Table 5. CCF experiment for the transition duct.

Sim	ϕ_{out}	α_L	α_T	Factors	Area-Averaged		Mass-Averaged		DPCPAV	Angle	Mach
					Recov	Cp	Recov	Cp			
a	32	-5	-5	-1 -1 -1	0.9765	0.6252	0.9757	0.6220	0.0215	7.83	0.1857
b	32	-5	5	-1 -1 1	0.9741	0.5916	0.9733	0.5888	0.0228	8.68	0.1900
c	32	0	0	-1 0 0	0.9756	0.6117	0.9748	0.6086	0.0217	9.41	0.1882
d	32	5	-5	-1 1 -1	0.9769	0.6269	0.9761	0.6244	0.0207	10.07	0.1869
e	32	5	5	-1 1 1	0.9761	0.6187	0.9754	0.6156	0.0210	10.34	0.1867
f	52	-5	0	0 -1 0	0.9809	0.6858	0.9798	0.6802	0.0153	10.82	0.1839
g	52	0	-5	0 0 -1	0.9819	0.6964	0.9808	0.6914	0.0140	10.87	0.1838
h	52	0	0	0 0 0	0.9814	0.6889	0.9803	0.6840	0.0148	11.31	0.1834
i	52	0	5	0 0 1	0.9803	0.6738	0.9793	0.6706	0.0154	11.84	0.1848
j	52	5	0	0 1 0	0.9813	0.6877	0.9803	0.6835	0.0142	11.89	0.1834
k	72	-5	-5	1 -1 -1	0.9735	0.5984	0.9718	0.5940	0.0216	9.99	0.1891
l	72	-5	5	1 -1 1	0.9627	0.4324	0.9608	0.4275	0.0300	9.50	0.2216
m	72	0	0	1 0 0	0.9790	0.6626	0.9774	0.6580	0.0161	11.77	0.1851
n	72	5	-5	1 1 -1	0.9735	0.5977	0.9718	0.5933	0.0216	9.94	0.1892
o	72	5	5	1 1 1	0.9821	0.6989	0.9806	0.6931	0.0120	13.41	0.1836
p	50	0	0	-	0.9808	0.6821	0.9797	0.6773	0.0154	10.98	0.1838

The results for the performance measures of the 15 CFD simulations are also presented in Table 5. The main responses examined were the mass-averaged total pressure recovery, static pressure coefficient C_p, and total pressure distortion (DPCPAV). The Design Expert software package was used to perform the statistical analysis. The

statistical analysis indicated that there was too much noise in the responses to make any response surface model significant. This can be seen in Fig. 10 that shows the distribution of the total pressure recovery and static pressure coefficient (C_p) as a function of the outflow offset angle. At 72 degrees, there is significant noise in the recovery. The fact that a statistical quadratic model could not be generated does not lessen the impact of the statistical analysis. The statistical analysis provided the correct interpretation of the data – that there was too much noise in the data (specifically at 72 degrees) to statistically differentiate between some of the results.

When the low and high values at 72 degrees were temporarily substituted with values approximately near the average, a statistical quadratic model could be generated. The finding of that model was that the sidewall angles at the outflow (α_{outL} and α_{outT}) were not significant factors. That only left the ϕ_{out} as the significant factor. If each of the recoveries and pressure coefficients at 32, 52, and 72 degrees were averaged, the plots would look like Fig. 11. A quadratic curve was fit to those three points. The ϕ_{out} for the maximum recovery was 49.96 degrees with maximum recovery of 0.9802. The ϕ_{out} for the maximum static pressure coefficient was 50.83 degrees with a maximum static pressure coefficient of 0.6823.

Some judgment is needed in selecting the "optimum" configuration. The responses showed variations; however, at ϕ_{out} = 52 degrees, the variation in recovery and C_p seemed the least with a slight peak. It was decided to establish the "optimum" configuration to be ϕ_{out} = 50 degrees, α_L = 0.0 degrees, and α_T = 0.0 degrees.

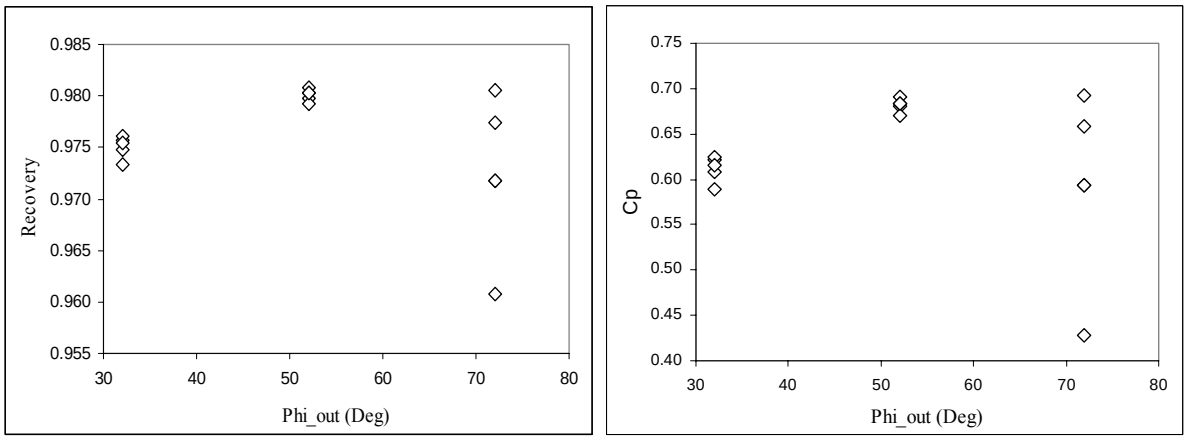

Figure 10. Total pressure recovery and pressure coefficient with respect to ϕ_{out}.

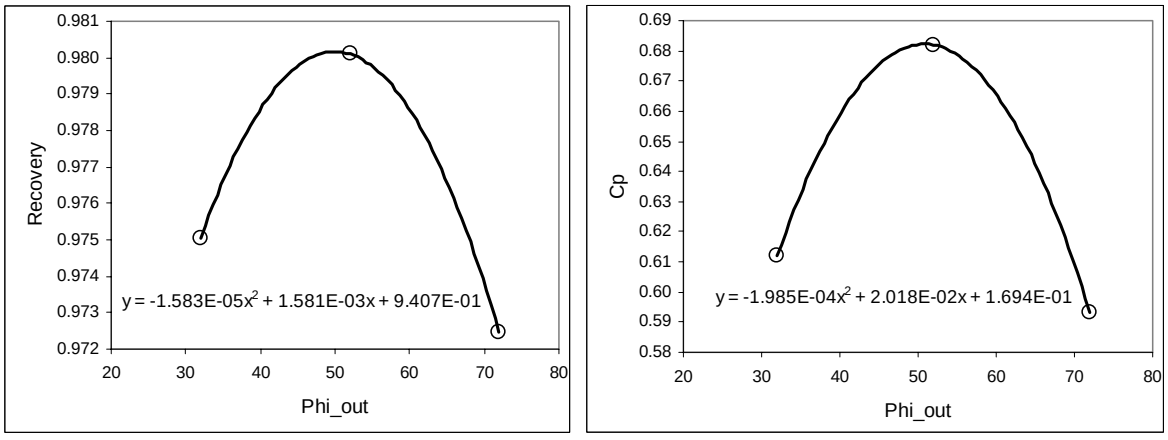

Figure 11. Quadratic fits of averages of total pressure recovery and pressure coefficient.

A CFD simulation was performed of the "optimum" configuration. The performance data is presented as Run p in Table 5. The differences between the performance measures of the CFD results and quadratic fit are likely due to noise. Table 6 compares the optimum configuration to the baseline configuration. The results indicate that the DoE study has lead to a transition duct with a significant increase in performance.

Table 6. Comparison of the baseline and optimum transition ducts.

Design	ϕ_{out}	α_L	α_T	Area-Averaged		Mass-Averaged		DPCPAV	Flow Angle	Mach
				Recov	Cp	Recov	Cp			
Baseline	-22.41	0	0	0.9676	0.5055	0.9668	0.5029	0.0307	4.3194	0.1829
Optimum	50.00	0	0	0.9808	0.6821	0.9797	0.6773	0.0154	10.9808	0.1838

C. Final Duct Design

The final duct design study examined the choice of the optimum configuration obtained from the DoE design study using the inflow boundary conditions detailed in section V, which were finalized only after completion of the DoE study. It was assumed that the conclusions of the DoE study remained valid – that the sidewall outflow angles could be set to zero (α_L = 0.0 degrees and α_T = 0.0 degrees) and that the only significant design factor was the off-set angle of the outflow, $\phi_{outflow}$. Thus a series of CFD simulations were performed as a one-factor search for the transition duct that provided the best performance. To improve the resolution of the flow field, the number of circumferential grid points was increased from 117 to 155. Table 7 and Fig. 12 present the results of the simulations. Run Ig of Table 7 represents the baseline duct design.

The change in the inflow conditions resulted in a general decrease in the recovery and pressure coefficient of the design as compared to Tables 4, 5 and 6. Setting the local circumferential flow velocity equal to the rotor rotational speed and setting the radial flow angle to zero rather than aligning the flow angle with the inflow surfaces was found to have a substantial negative impact on the transition duct performance.

Figure 12 shows the plots of the variation of the performance measures with respect to the factor $\phi_{outflow}$. As can be seen, the recovery and pressure coefficient both have a mild peak around $\phi_{outflow}$ = 0 degrees with a steep decline after $\phi_{outflow}$ = 15 degrees. The optimum duct was chosen with $\phi_{outflow}$ = 0 degrees. This seemed to maximize total pressure recovery (92.7%) and static pressure coefficient (0.539), while keeping an acceptable margin from a drop in performance occurring after $\phi_{outflow}$ = 15 degrees. This computed total pressure loss of 7.3% compares well with the corresponding loss computed for the Allison duct 1b (upstream of the nozzle) of 6.9%. With the transition-duct area ratio of 2.09 (or Cp-ideal = 0.77 for uniform flow), the optimum diffuser effectiveness (Cp/Cp-ideal) of 70% is considered good given the severe inlet nonuniformity, the required flow turning, and the diffuser L/w of 3.3. The flow was successfully turned to nearly zero degrees (axial). The total pressure distortion was not minimized; however, the values were below acceptable limits. The coordinates for this duct were delivered to the mechanical designers for final mechanical design and fabrication.

Figure 13 provides a general view of the flow through the transition duct by showing the Mach number contours at a circumferential surface through the duct. Figure 14 shows the total pressure contours at the outflow of the transition duct. The optimum duct has slightly smaller low-total-pressure regions and high-total-pressure regions. The region of low total pressure is located near the hub surface and the region of high total pressure is located near the case surface. By varying the duct offset angle, the low total pressure region could have been placed at either the leading or trailing walls; in terms of the impact of turbine entry conditions on turbine performance, the radial distortion of the optimum duct was considered preferable to such circumferential nonuniformities.

Table 7. Final duct design.

Run	$\phi_{outflow}$	Recovery	Cp	DPCPAV	Exit Flow Angle
Ig	-22.41	0.9234	0.5069	0.0364	-0.2643
Id	-20	0.9239	0.5112	0.0358	-0.0790
Ic	0	0.9267	0.5394	0.0275	1.3882
If	8	0.9263	0.5388	0.0230	1.8667
Ie	15	0.9241	0.5246	0.0240	1.9862
Ia	35	0.8881	0.2570	0.0701	-1.5012
Ib	45	0.8717	0.1515	0.0818	-1.3436

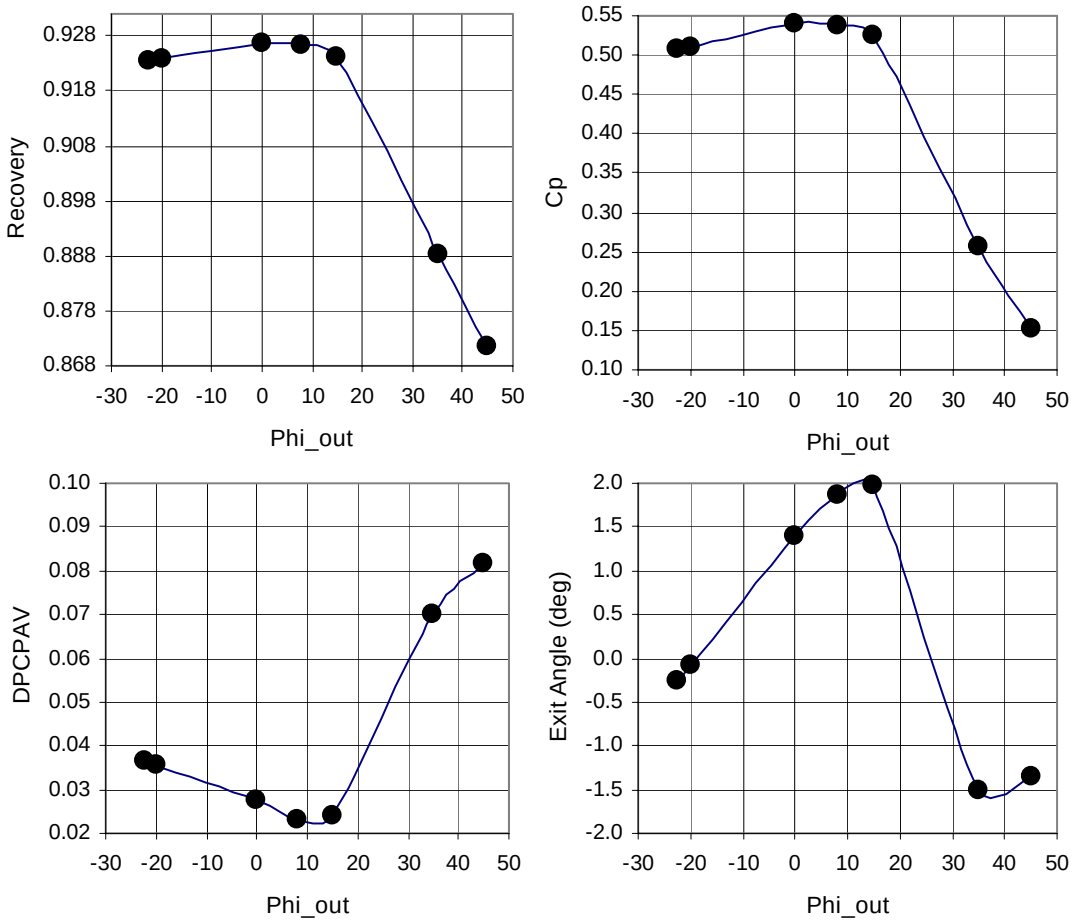

Figure 12. Performance of transition duct for final design study.

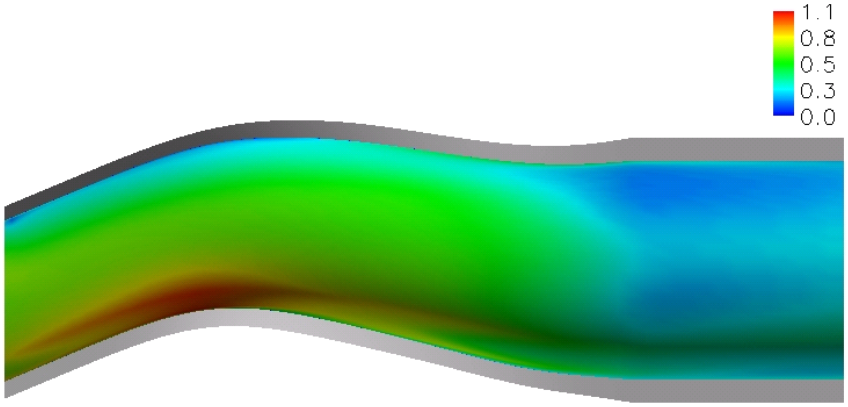

Figure 13. Mach number contours on a circumferential surface.

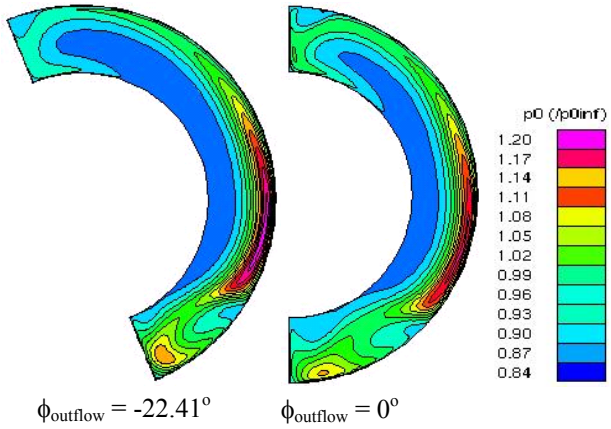

Figure 14. Total pressure contours at the outflow of the transition duct.

VII. Summary and Conclusion

Methods of computational fluid dynamics (CFD) and statistical design of experiments (DoE) were used to design a transition duct for a wave rotor rig. The characteristic of the duct was the diffusion of a non-uniform inflow in a partial-annular duct. The most significant design factor was the offset angle $\phi_{outflow}$ of the duct outflow. This factor was varied to obtain the optimum duct design. The transition duct has been fabricated and is scheduled to be tested in the NASA-Glenn wave-rotor component rig. While the experiment will mainly examine the behavior of the flow field ducted from the wave rotor, the experimental data will also provide an opportunity to validate the CFD methods. However, the CFD simulations indicated significant sensitivity to the choice of turbulence model and inflow conditions. These sensitivities will make performing validation studies a greater challenge than performing design studies since the level of uncertainty of the CFD methods may obscure the level of error between the CFD results and experimental data.

Acknowledgments

The authors are grateful for the support by the NASA Vehicle Systems Program (VSP), Low-Emissions Alternative Power (LEAP) Project, Alternative Propulsion Systems (APS) Element with Leo Burkardt as Element Manager.

References

[1]Welch, G.E., S.M. Jones, and D.E. Paxson, "Wave-Rotor-Enhanced Gas Turbine Engines," *J. Engineering for Gas Turbines and Power*, **119**, No. 2, April 1997, pp. 469-477..

[2]Gegg, S.G. and P.H. Snyder, "Aerodynamic Design of a Wave Rotor to High Pressure Turbine Transition Duct," AIAA-1998-3249, July 1998.

[3]Weber, K.F. and P.H. Synder, "Wave rotor to High Pressure Turbine Transition Duct Flow Analysis," AIAA-1998-3250, July 1998.

[4]Society of Automotive Engineers (SAE), "Gas Turbine Engine Inlet Flow Distortion Guidelines," SAE ARP 1420, Rev. B, February 2002.

[5]Mani, M., A. Cary, and S. Ramakrishnan, "A Structured and Hybrid-unstructured Grid Euler and Navier-Stokes Solver for General Geometry," AIAA-2004-0524, January 2004.

[6]Paxson, D. E., "Comparison Between Numerically Modeled and Experimentally Measured Wave-Rotor Loss Mechanisms," *J. Propulsion and Power*, **11**, No. 5, Sept.-Oct., pp. 908-914, 1995.

[7]Montgomery, D.C., Design and Analysis of Experiments, John Wiley & Sons, Inc., New York, 2001.